molecules

MDPI

Article

In Situ Synthesis of 3D BiOCl–Graphene Aerogel and Synergistic Effect by Photo-Assisted Activation of Persulfate for Methyl Orange Degradation

Yukun Li [1,*], Dan Zhang [2], Yongshu Zhang [1], Cong Chao [1], Qishi Chen [1], Sen Yao [1] and Cuixia Liu [1]

[1] School of Energy and Environmental Engineering, Zhongyuan University of Technology, Zhengzhou 450007, China
[2] Science and Technology Innovation Coordination Service Center of Laiwu District, Jinan 271100, China
* Correspondence: 6750@zut.edu.cn

Abstract: BiOCl/graphene aerogel graphene (BGA) was successfully obtained by in situ hydrothermal synthesis, and the chemical, structural, morphological, and photocatalytic properties were systematically characterized. BGA with the doping amount of BiOCl at 20% (BGA-4) exhibited the optimal activation efficiency for persulfate (PDS) on the degradation of methyl orange (MO) under simulated sunlight (SSL) illumination as compared to the pure graphene (GA) and aerogel composites with different BiOCl content. The influence of various reaction parameters on the MO removal efficiency, such as the reaction system, catalyst activator dose, PDS concentration, BiOCl doping amount, and the initial pH of the solution, was investigated. Under optimum conditions, the catalytic efficiency of BiOCl-doped GA with the mass ratio of 20% (BGA-4) was 5.61 times that of GA. The strengthening effect of BGA-4 benefited from the synergistic effect of $^1O_2$, $O_2{\cdot}^-$ and the generation and rapid electron transfer of photo-induced electron (e^-) in the BGA-4/SSL/PDS system. Considering the superior stability and recyclability of BGA-4, the BGA-4/SSL/PDS system exhibits great potential in actual wastewater treatment.

Keywords: persulfate; graphene aerogel; photocatalytic activation; BiOCl; simulated sunlight

check for updates

Citation: Li, Y.; Zhang, D.; Zhang, Y.; Chao, C.; Chen, Q.; Yao, S.; Liu, C. In Situ Synthesis of 3D BiOCl–Graphene Aerogel and Synergistic Effect by Photo-Assisted Activation of Persulfate for Methyl Orange Degradation. *Molecules* **2023**, *28*, 4964. https://doi.org/10.3390/molecules28134964

Academic Editor: Isabella Natali Sora

Received: 15 May 2023
Revised: 6 June 2023
Accepted: 22 June 2023
Published: 24 June 2023

Copyright: © 2023 by the authors. Licensee MDPI, Basel, Switzerland. This article is an open access article distributed under the terms and conditions of the Creative Commons Attribution (CC BY) license (https://creativecommons.org/licenses/by/4.0/).

1. Introduction

Water is the indispensably precious resource that mankind depends on for existence and development [1]. By the year 2025, the number of people who lack access to safe drinking water is estimated to be more than 2 billion; nearly 20% of the global population will be living in countries or regions with absolute water scarcity [2,3]. Unfortunately, rapid economic development, industrialization, and urbanization have exacerbated water shortages and water quality degradation. Particularly, the enrichment of textile printing and dyeing wastewater possesses a remarkable effect on the water ecosystem and food chain. More seriously, azo dye wastewater not only affects the germination and growth of plant seeds but also has carcinogenic, teratogenic, and mutagenic effects on humans and animals health [4]. Thus, increasing studies have placed emphasis on the decomposition of azo dye wastewater through an efficient method in recent years. The traditional treatment methods of azo dye wastewater, such as biodegradation [5], physical adsorption [6], and ozonation [7], have been widely employed in research and development. Recently, many researchers have paid more attention to advanced oxidation processes (AOPs) which degrade azo dye into harmless inorganic matters via redox reaction. Among the reported available AOPs, Fenton or Fenton-like technology is an effective method for degrading refractory organic pollutants. However, the narrow acidic operation pH, unrecyclable catalysts, and the production of iron sludge are the limiting factors for scale application of Fenton or Fenton-like technology [8]. Recently, sulfate radicals ($SO_4{\cdot}^-$) activated

by persulfate (PS) have attracted extensive attention due to their high redox potential of 2.5–3.1 V, which is comparable to hydroxyl radicals (·OH, 2.8 V) [9]. The oxidation-reduction potential, environmental friendliness, and selectivity for removing refractory organic pollutants attributed to the redox properties of PS make it possible for a viable alternative to replace H_2O_2 [10,11]. However, the oxidation property of PS itself is not prominent, and the performance could be strengthened by means of activation [12].

$SO_4\cdot^-$could be generated efficiently by activating peroxide bonds in PS using external energy (heat, ultrasound, UV irradiation, or microwave), metallic materials (mostly transition metals), and non-metallic materials (carbon-based material materials, quinones, or strong alkaline) [13]. Among these methods, physical activation is energy-intensive, and metal-based catalysts may cause the release of metal ions [14]. Recently, the carbon-based materials have made significant progress in the activation of PS in terms of its low cost and electrical conductivity [15]. Graphene is a honeycomb-like sheet of carbon, just one atom thick, with the excellent features of large specific surface area, high electrical and thermal conductivity, and mechanical properties [16]. It was first reported that reduced graphene oxide (rGO) could activate PMS to generate $SO_4\cdot^-$, and the catalytic performances of rGO could be enhanced with the increase in oxygen containing groups [17]. However, the separation of the powdered rGO is time-consuming and costly. The graphene aerogel with three-dimensional (3D) structure prepared from graphene nanosheets by certain method can resolve the catalyst recovery and secondary pollution problems. Previous study by Karbasi et al. [18] showed that macroscopic rGO aerogels played an important role in inducing highly efficient radicals through PMS activation. It is a good choice to construct semiconductor composites based on aerogel. Ma et al. reported that carbon aerogel/TiO_2 composite material is a promising photocatalysts for environmental pollutants degradation owing to the decreased recombination probability of photo-induced carriers [19]. The abundant pore structure and large surface area of 3D graphene aerogel make semiconductor materials uniformly disperse on the surface of graphene. The black body and surface sensitization would be conducive to promote the visible optical absorption and the charge transportation and separation. Cu_2O/rGO aerogel showed superior photocatalytic activity in MO degradation owing to the broadening light absorption capability [20]. Chen et al. [21] demonstrated that 3D Ag/Ag@Ag_3PO_4/GA exhibited excellent degradation efficiency of organic dye contaminants in the visible light. BiOCl, with a tunnel-like structure, has been regarded as a new type of photocatalytic or catalytic materials in recent years [22,23]. Due to the enhanced visible-light response and efficient separation of electron and hole, BiOCl/rGO aerogel, fabricated by a chemical reduction self-assembly method at 180 °C for 6 h, displayed an outstanding synergistic effect on the adsorption and photocatalytic degradation of oxytetracycline [24]. BiOCl/rGO aerogel was prepared via a combined hydrothermal method with vacuum freeze drying [25]. However, the combination of BiOCl using $BiCl_3$ as raw material with graphene to fabricate 3D aerogel without the vacuum freeze-drying process for the treatment of MO wastewater by activating PDS has rarely been reported under simulated sunlight irradiation.

Herein, a series of BiOCl/GA hybrid architectures with different BiOCl contents were successfully synthesized via an in situ hydrothermal method followed by natural drying. The physicochemical properties and photoelectrochemical properties of BiOCl/GA composites were systematically examined by a range of characterization techniques, and the catalytic activity of BiOCl/GA composites was evaluated by activating PDS for MO degradation. The experiments under different conditions, such as BiOCl ratio, pH, PDS concentration, activator dosage, and co-existing anions, were conducted to study the influence on the removal of MO in the presence of simulated sunlight irradiation. Moreover, the recycling experiment was also used to evaluate the stability of BiOCl/GA in PDS oxidation system. In addition, a free radical capture experiment was further undertaken to identify the dominant reactive species.

2. Results and Discussion

2.1. Crystal Structure of Fibers of BGA-4

XRD is an effective method for evaluating the crystalline properties of composites. The XRD patterns of GO, GA, and BGA were illustrated in Figure 1. As presented in Figure 1a, the peak of GA appeared at about 2θ = 24°; meanwhile, the characteristic peak at 2θ = 11.6° disappeared, indicating that most oxygen-containing functional groups belongs to GO were reduced successfully. As shown in Figure 1b, the distinctive peaks at 11.9°, 25.9°, 32.5°, 33.4°, 36.5°, 40.9°, 46.6°, 49.7°, 54.1°, and 58.6° of BGA were perfectly consistent with (001), (101), (110), (102), (003), (112), (200), (113), (211), and (212) planes of the tetragonal phase of BiOCl (JCPDS 06-0249), respectively. Furthermore, the peak intensity of BGA was directly proportional to the content of BiOCl (≤15%), which indicated that the graphene had no effect on the growth orientation of BiOCl but did restrain the growth of BiOCl crystal in some degree [26]. As the content of BiOCl increases, four characteristic peaks of BGA-4 and BGA-5 at 2θ of 27.3°, 38.1°, 39.7°, and 48.7° were subordinated to (012), (104), (110), and (202) crystal planes of Bi metal (JCPDS card No. 44-1246), which demonstrated a small quantity of Bi^{3+} being reduced to metal Bi.

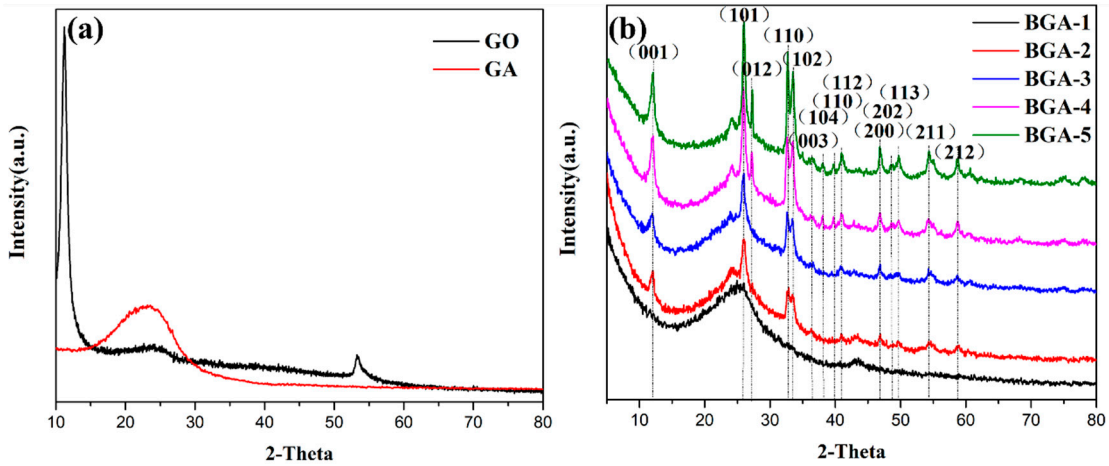


Figure 1. XRD patterns of GO and GA (**a**), BGA-1, BGA-2, BGA-3, BGA-4, and BGA-5 composites (**b**).

Raman spectra were used to analyze the chemical structure of GA and BGA-4. As presented in Figure 2a, two characteristic peaks occurred at 1344 cm^{-1} and 1582 cm^{-1}, which belonged to the D and G bands of graphene. The D peak, reflecting the defects and disorder of crystal, represents the sp^3 hybrid structure or the sp^2 bond hybrid defect graphene edge structure. The G peak is generated by the stretching motion of all sp^2 atom pairs [27]. The ratios of D band to G band intensity (ID/IG) for GA and BGA-4 were 1.16 and 1.22, indicating that BGA-4 had a higher defects and disorders degree than GA, which suggested that BiOCl has a remarkable disruption of symmetrical lattice for BGA composites.

FT-IR spectroscopy was used to explore the chemical structure of the GO, GA, and BGA-4. As displayed in Figure 2b, the peaks of GO at about 1059 cm^{-1}, 1229 cm^{-1}, 1400 cm^{-1}, 1618 cm^{-1}, 1734 cm^{-1}, and 3419 cm^{-1} correspond to the antisymmetric and symmetric stretching vibrations of C-O-C, C-OH, O-H, C=C, carbonyl C=O, and O-H tensile vibration of H_2O molecules absorbed to the surface, respectively [28]. These oxygen-containing functional groups became weaker or even disappeared in GA and BGA compared to the GO spectrum, confirming the efficient reduction of GO. Owing to the low content of BiOCl, the typical mode of Bi-O was far too subtle to be observed at 536.1 cm^{-1} in the spectrum of BGA [29].

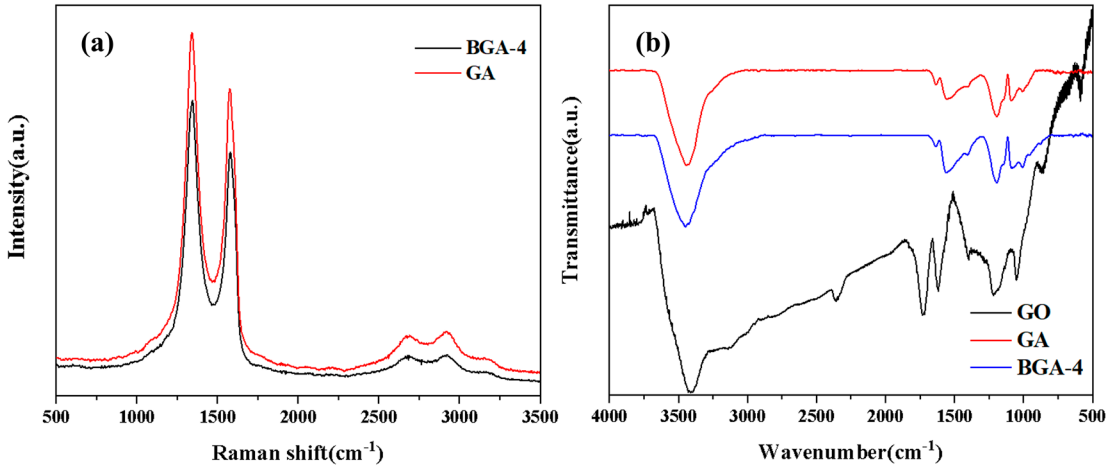


Figure 2. Raman analysis (**a**) of the prepared GA and BGA-4, and FTIR spectra (**b**) of the prepared GO, GA, and BGA-4.

The elemental composition and chemical properties on the surface of the BGA-4 were determined by X-ray photoelectron spectroscopy (XPS). As reflected in Figure 3a, the peaks of Bi 5d, Bi 4f, Bi 4d, Bi 4p, Cl 2p, C 1s, and O 1s appeared in the survey scan spectra of BGA-4, which indicated that BiOCl had been successfully introduced into BGA-4. The high-resolution XPS spectra of C1s was shown in Figure 3b; the C 1s peak of BGA-4 was fitted into four peaks at about 284.6 eV, 284.9 eV, 286.0 eV, and 288.9 eV, corresponding to C-C, C-O, C-OH, and O=C-O bonds, respectively. The results indicated that some of the oxygen-containing groups on GO were retained in the process of BGA-4 synthesis, which may be beneficial for the activation of PDS. Two characteristic peaks (Figure 3c) at 159.7 eV and 165.0 eV were ascribed to Bi 4f 5/2 and Bi 4f 7/2, indicating the existence of Bi^{3+} in BGA-4 [30]. As shown in Figure 3d, the O 1s core-level spectrum of BGA-4 could be mainly divided into two peaks at about 531.5 and 533.7 eV, corresponding to the Cl–O and C–O bonds in XPS [31]. The high-resolution Cl 2p spectra (Figure 3e) including two obvious characteristic peaks at 198.6 eV and 200.2 eV were ascribed to Cl 2p 1/2 and Cl 2p 3/2, indicating the existence of BiOCl in BGA-4.

EIS was conducted to clarify the contribution of BiOCl on the conductivity and charge carrier transfer of BGA-4. As illustrated in Figure 3f, the Nyquist plots were a sort of combination of semicircles and straight lines. The arc radius of the Nyquist circle reflected the charge transfer resistance. Smaller charge transfer resistance might be conducive to the separation and transfer efficiency of the optical carrier [32,33]. The ohmic resistance (R_S) and the charge transfer resistance (R_{CT}) of BGA-4 were 39.73 Ω and 54.15 Ω, substantially lower than those of GA (42.26 Ω and 111.74 Ω), which indicated that BiOCl could improve the conductivity and electron transfer capacity of BGA-4 composite. The rapid electrolyte ion transport to the active sites and the enhanced separation of photoelectrons from vacancies might be conducive to PDS activation.

The UV–Vis DRS of the pristine BiOCl, GA, and BGA-4 are exhibited in Figure 4a. It can be seen that BiOCl possesses a steep absorption edge at about 369 nm, which was consistent with the band gap (3.36 eV) estimated based on the formula of $Eg = 1240/\lambda_g$ (eV). However, GA and BGA-4 demonstrated strong absorption in the whole visible light region because of the surface sensitization and black-body property of aerogel [34]. The strong capacity of light absorption was conducive to remove MO by photo-assisted activation of PDS.

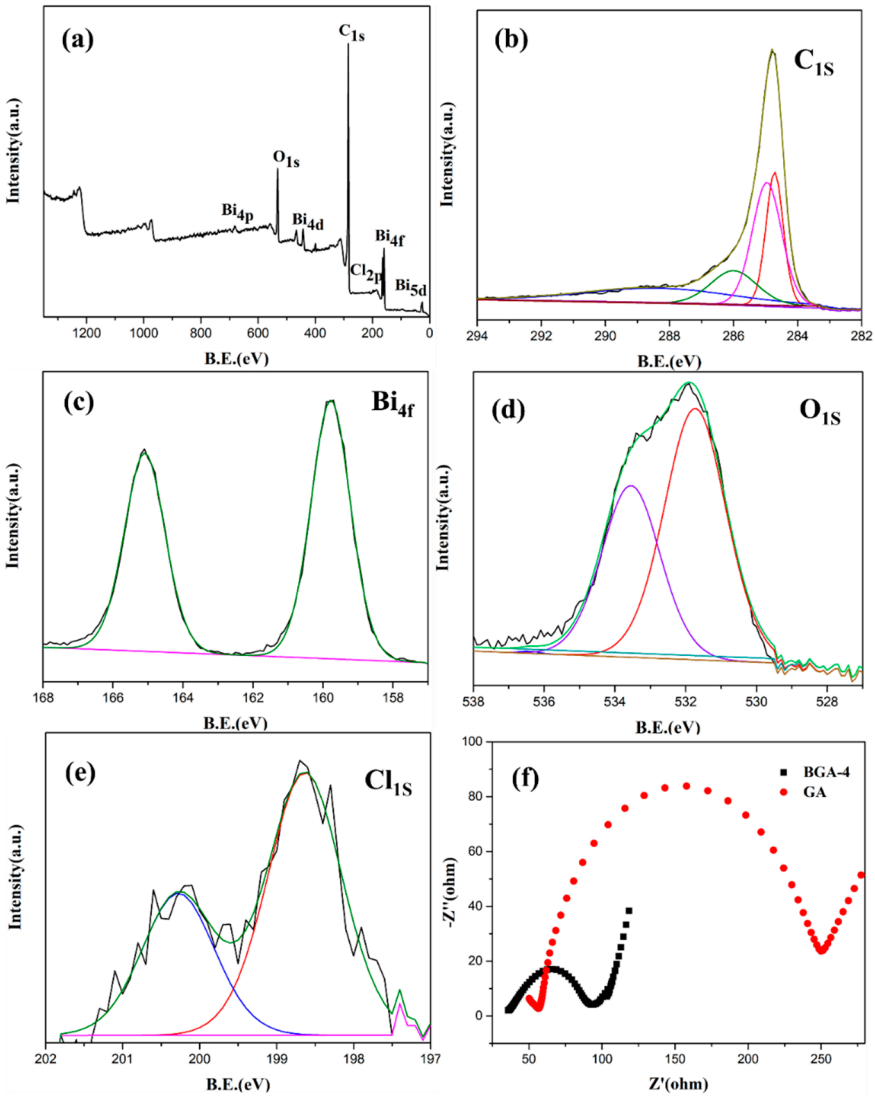


Figure 3. XPS spectra of the survey (**a**), C_{1s} (**b**), Bi_{4f} (**c**), O_{1s} (**d**), and Cl_{1s} (**e**) for BGA-4 composite, and EIS (**f**) of GA and BGA-4.

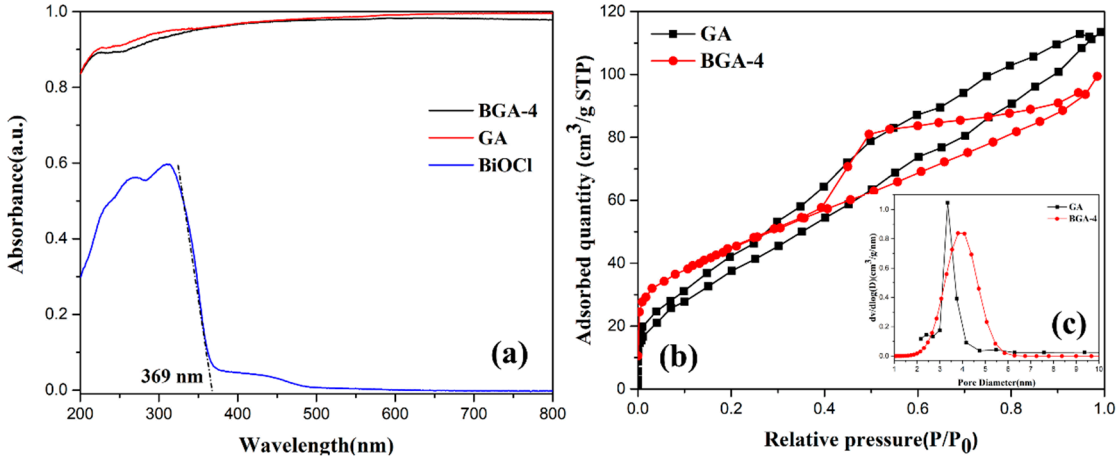


Figure 4. UV–Vis DRS of BiOCl, GA, and BGA-4 (**a**), N_2 adsorption–desorption isotherms (**b**), and pore size distribution plots (**c**) of GA and BGA-4.

SEM was exploited to characterize the morphology of the prepared GA and BGA-4. Figure 5a–c represented that GA still exhibited the layered structure of graphene sheets and then folded into a multiporous network structure. As displayed in Figure 5d–f, the SEM images of BGA-4 showed that the 3D flower-like uniformly microspheres (1–2 μm) were successfully doped into the surface or internal cavities of BGA-4, indicating the successful synthesis of BGA-4 using GO and $BiCl_3$ as raw materials.

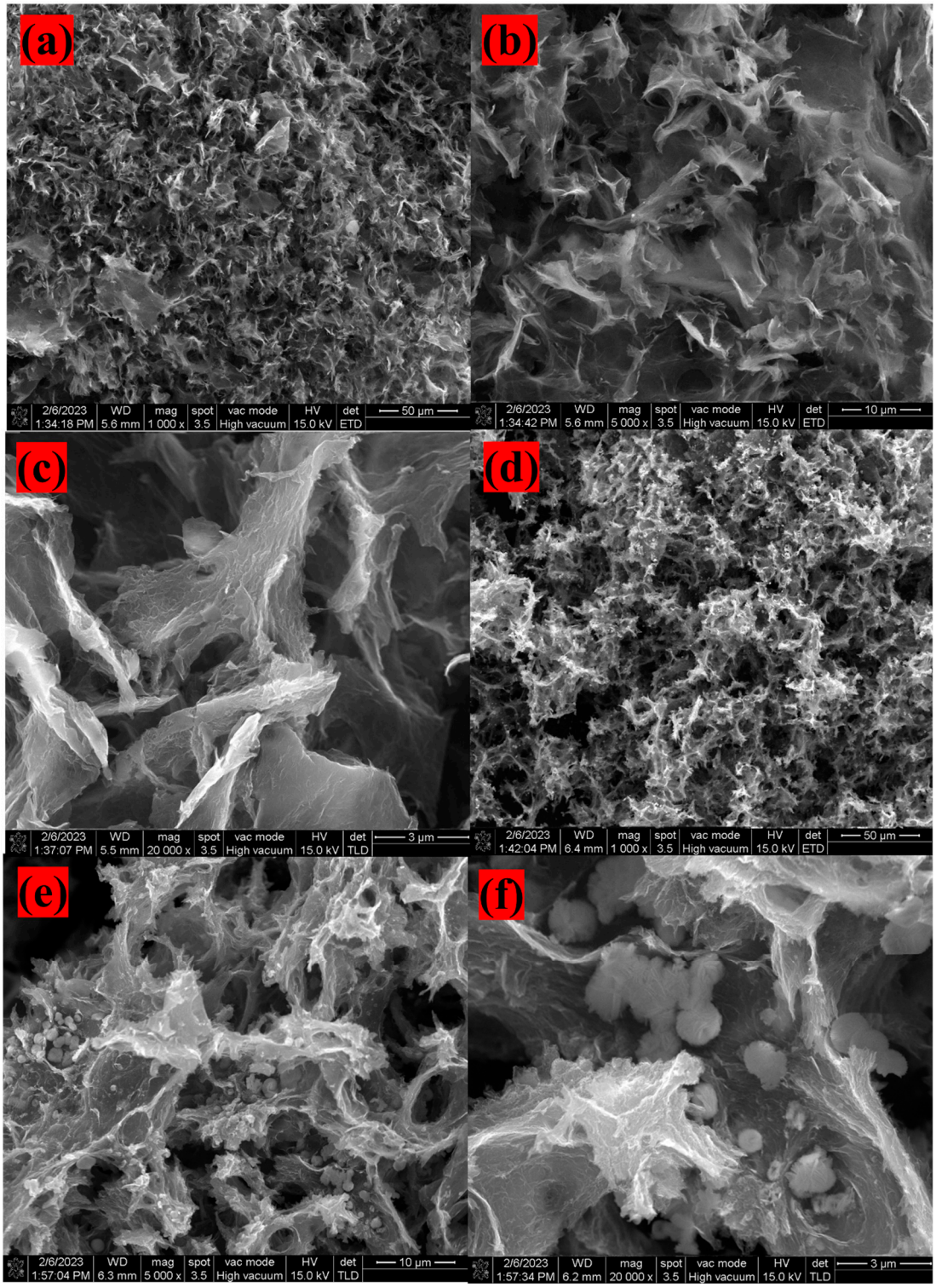


Figure 5. SEM images of GA (**a**–**c**) and BGA-4 (**d**–**f**).

The EDS results (Figure 6) of BGA-4 clearly demonstrated the presences and spatial distributions of C, Bi, Cl, and O elements (Figure 6c–f), further demonstrating the successful hybridization of BGA-4. The content of major elements (C, Bi, Cl, and O) was 76.50%, 7.44%, 0.8%, and 15.26%, respectively. The atomic number ratio of Bi/Cl was 1.6:1, which demonstrated that most bismuth existed in the form of BiOCl, and perhaps other forms exist. The results are consistent with findings in XRD patterns, as illustrated in Figure 1.

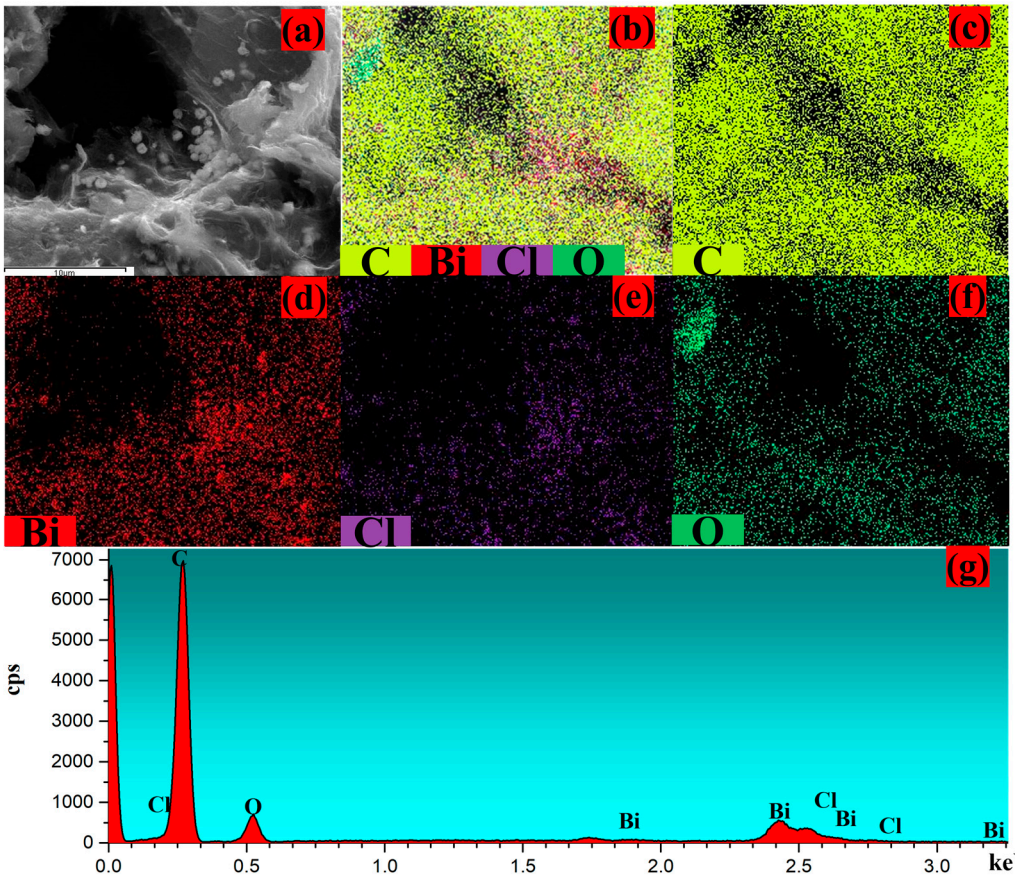


Figure 6. SEM image (**a**), elemental mapping (**b**–**f**), and EDS spectra (**g**) of BGA-4.

2.2. Comparative Tests on MO Removal

The batch experiments on MO degradation were implemented under simulated sunlight and PDS oxidative environment, respectively. As illustrated in Figure 7a, MO loss by PDS (22.8%), GA/PDS (31.8%), SSL/PDS (28.4%), and GA/SSL/PDS (40.1%) systems were both less than 50% within 60 min, which indicated that PDS was not easily activated by simulated sunlight, but could be decomposed to produce $SO_4 \cdot^-$ by the lone pairs of electrons belonging to C=O of GA [36]. Meanwhile, it can be observed that the removal efficiency of MO was 40.1%, 22.2%, 72.4%, and 89.9% in the GA/SSL/PDS, BGA-4/SSL, BGA-4/PDS, and BGA-4/SSL/PDS systems, respectively. The results revealed that graphene aerogel composites decorated with BiOCl would expose more active sites on the catalyst surface to the target contaminant. Moreover, the decontamination of MO may also be ascribed to the photo-induced e^-/h^+ pairs to SSL irradiation and the efficient electron transfer and adsorption of both PDS and the contaminant onto active sites in the BGA-4/SSL/PDS system [37,38]. As shown in Figure 7b, the MO removal behavior in vitro followed the first order kinetic equation (R^2>0.95). The apparent reaction rate constants (K_{obs}) for MO degradation were 6.35 × 10^{-3} min^{-1} (GA/SSL/PDS), 5.08 × 10^{-3} min^{-1} (GA/PDS), 4.95 × 10^{-3} min^{-1} (SSL/PDS), 4.39 × 10^{-3} min^{-1} (PDS), 3.56 × 10^{-2} min^{-1} (BGA-4/SSL/PDS), 2.86 × 10^{-3} min^{-1} (BGA-4/SSL), and 1.80 × 10^{-3} min^{-1} (BGA-4/PDS)

in different systems, respectively. The experiment results demonstrated that the MO degradation rate by BGA-4 composite was 5.61 times that of GA in PDS activation under simulated sunlight irradiation.

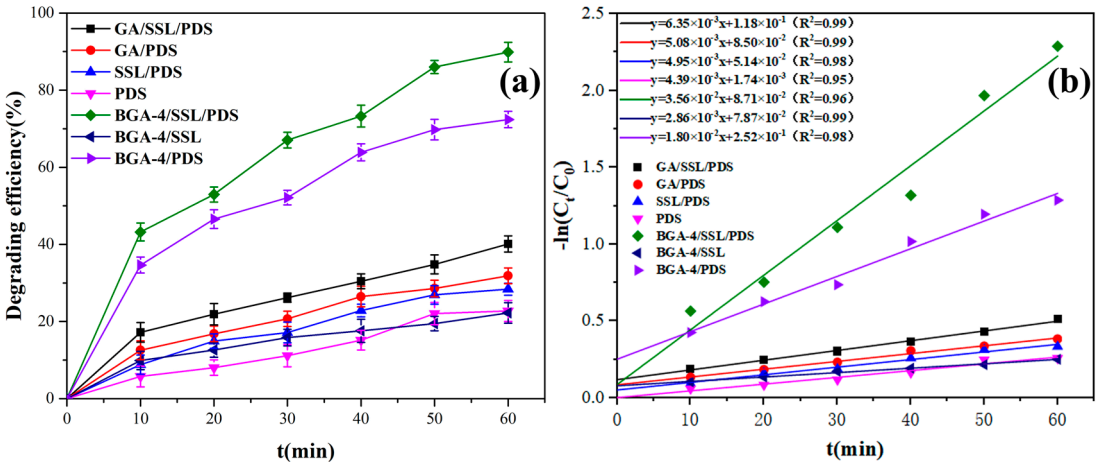


Figure 7. MO decontamination efficiency (**a**) and pseudo-first-order plots (**b**) of MO degradation over various processes (reaction conditions: 0.4 g/L catalyst, 75 mg/L PDS, 300 W xenon lamp, and C_0 = 15 mg/L).

2.3. Parameters Impacting MO Degradation by the BGA-4/SSL/PDS System

2.3.1. Effect of the Catalyst BGA-4 Concentration

BGA-4 dosage exhibited a significant effect on MO removal (Figure 8a). When the dosage increased from 0.2 g/L to 0.6 g/L in the BGA-4/SSL/PDS system, the removal efficiency of MO was 53.3% (0.2 g/L), 70.7% (0.3 g/L), 89.9% (0.4 g/L), 91.5% (0.5 g/L), and 92.3% (0.6 g/L) within 60 min, respectively. The degradation efficiency was significantly enhanced with the BGA-4 concentration increasing from 0.2 g/L to 0.4 g/L, which might be attributed to the enhanced proteolytic activity and surface area for the effective activation of PDS. However, the degradation efficiency of MO increased slowly at higher dosages (>0.4 g/L), suggesting that PDS played an important role in MO degradation when the activator was sufficient. Thus, the concentration of activator was set to 0.4 g/L for the follow-up experiments.

2.3.2. Effect of PDS Concentration

The effect of PDS concentration on MO degradation was evaluated in Figure 8b over the BGA-4/SSL/PDS system. The removal efficiency of MO was 44.7%, 68.3%, 89.9%, 92.1%, and 94.5%, when the PDS concentration was set to 15 mg/L, 45 mg/L, 75 mg/L, 105 mg/L, and 135 mg/L, respectively. The removal efficiency of MO increased from 44.7% to 94.5% within 60 min, indicating that it is advantageous to add PDS in MO degradation. The reason may be that high concentration of PDS generated more active species in the reaction system. PDS acted as electron acceptor could reduce O_2 to $O_2{\cdot}^-$ [39], and $O_2{\cdot}^-$ reacted with some of PDS to form $SO_4{\cdot}^-$ [40]. While the concentration of PDS progressively increased from 75 mg/L to 135 mg/L, the degradation rate of MO leveled off, perhaps related to a finite number of photoelectrons. After comprehensive consideration, the optimal concentration of PDS was selected as 75 mg/L.

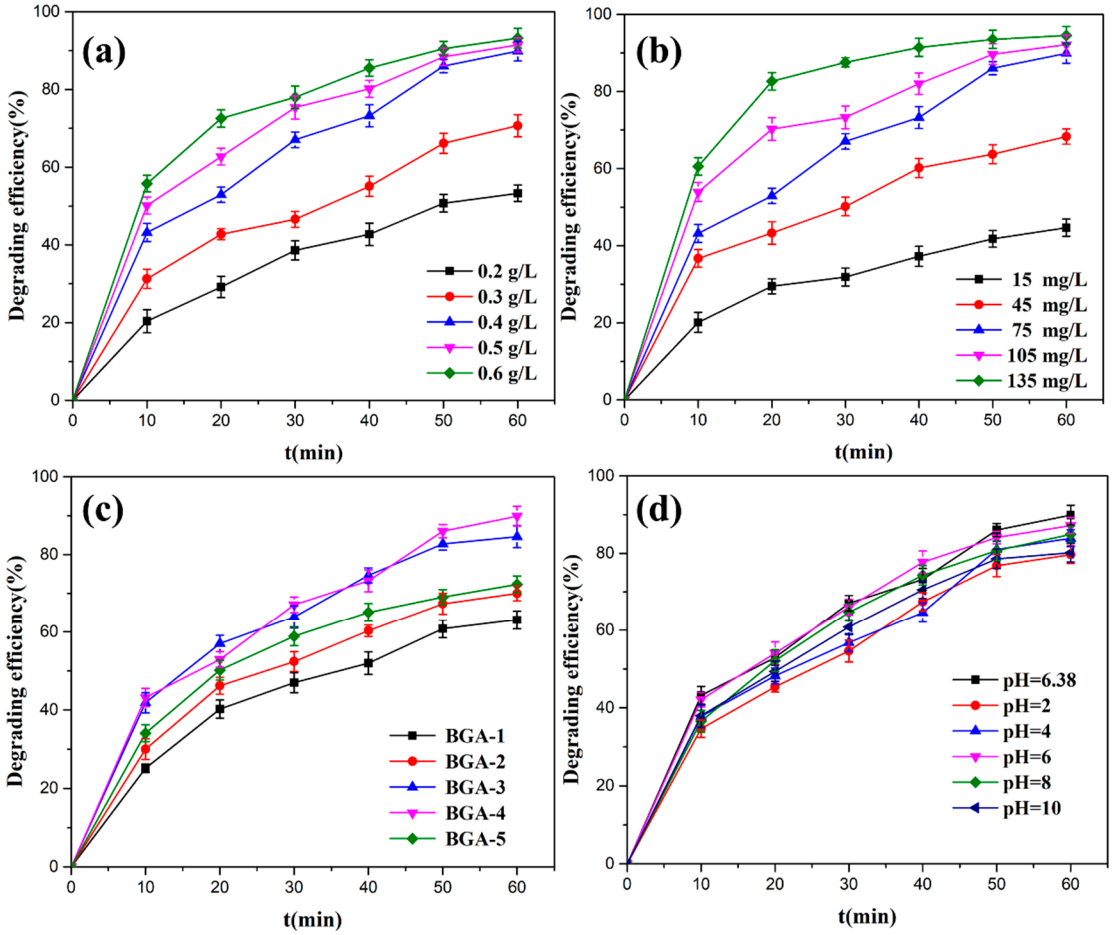


Figure 8. Effect of BGA-4 dosage (**a**), PDS concentration (**b**), BiOCl doping amount (**c**), and initial pH (**d**) on the degradation of MO.

2.3.3. Effect of BiOCl Doping Amount

The effect of BiOCl concentration in aerogel composites on MO degradation was exhibited in Figure 8c. BGA-4 displayed the highest degradation efficiency of 89.9%. As the corresponding mass ratio of BiOCl increased from 5% to 20%, the degradation efficiency of MO increased from 63.1% to 89.9%. The reason might be that more BiOCl can produce more photoelectrons and holes, thus promoting the activation of PDS to produce more free radicals. It was worth noting that if the amount of BiOCl further increased to 25%, the degradation efficiency of MO dropped to 72.3%. The result implied that BiOCl content was a key factor for improving the photocatalytic activity of aerogel composites [41]. Therefore, the optimal mass ratio of BiOCl for this study was set at 20%.

2.3.4. Effect of pH

The photocatalytic degradation of MO was greatly influenced by the solution pH in the BGA-4/SSL/PDS system. As displayed in Figure 8d, the removal efficiencies of MO were 79.7% (pH = 2), 83.9% (pH = 4), 87.2% (pH = 6), 84.9% (pH = 8), and 80.2% (pH = 10), respectively. Higher or lower pH of the solution was detrimental to the degradation efficiency of MO, which might be attributed to the scavenging effect of H^+ on the activity factor at lower pH and less efficiency in the generation of the reactive species at higher pH [38], while the highest degradation rate of MO was obtained at pH 6. In general, BGA-4 exhibited a high removal rate of MO across a broad range of pH in the BGA-4/SSL/PDS system. Since the pH of the MO solution (6.23) is closer to 6, the whole experiment is carried out without pH adjustment.

2.4. Effect of Co-Existing Components

In practical wastewater, the presence of inorganic anions printing and textile auxiliaries, such as HCO_3^-, Cl^-, citrate, and sodium dodecyl benzene sulfonate (SDBS), is obvious. Usually, these co-existing anions showed inhibition towards the removal of MO in the following ways by rapidly reacting with the free radicals and by changing the acidic/basic conditions [42]. As displayed in Figure 9a, the degradation of MO was inhibited by the co-existing anions (10 mM) to varying degrees. The presence of HCO_3^- (82.1%) had a passive effect on the degradation of MO, probably because the increased pH that could restrain the generation of activity factors. The removal rate of MO fell to 47.7% because of the h^+ captured by sodium citrate in the BGA-4/SSL/PDS system. Generally, Cl^- could react with $SO_4\cdot^-$ or ·OH to form Cl·, whose oxidation susceptibility is relatively weak. The generation of $O_2\cdot^-$ was suppressed because of the dissolved oxygen reduced by the bubbles generated from SDBS, thus causing the removal ratio of MO to be pared down to 42.3%.

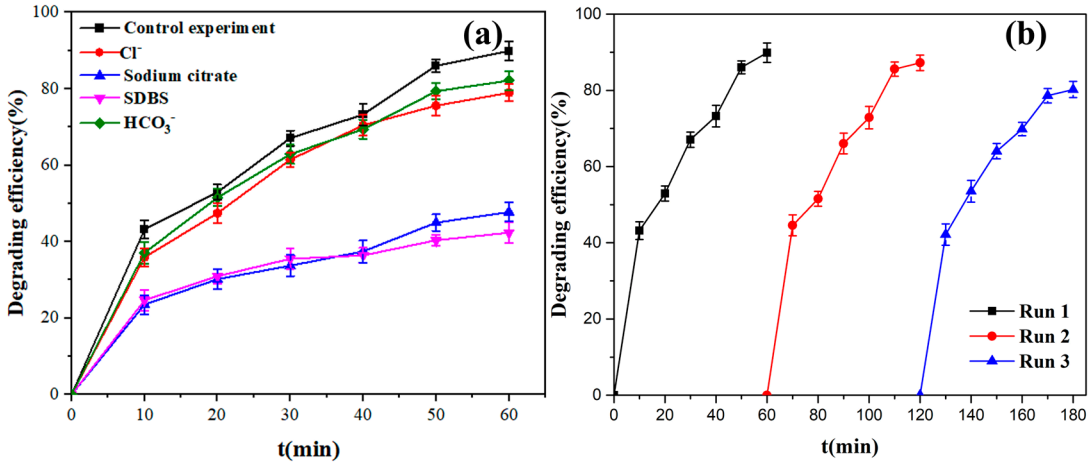


Figure 9. Effect of coexisting ions (**a**) and the reusability potential (**b**) of as-prepared catalyst in the BGA-4/SSL/PDS system (reaction conditions: 0.4 g/L BGA-4, 75 mg/L PDS, 300 W xenon lamp, and C_0 = 15 mg/L).

2.5. Recycling Studies

The recycling and stability of BGA-4 for PDS activation with the optimized dosages was evaluated through three cycles of experiments. The used BGA-4 was washed simply with deionized water and ethanol 2−3 times before each experiment started. As shown in Figure 9b, the MO removals in three experiments were 89.9%, 87.2%, and 80.2% in the BGA-4/SSL/PDS system, respectively. The degradation rate of MO decreased because the active sites reduced by MO and byproducts remained on the surface of BGA-4 via van der Waals interaction force [43]. The experimental results demonstrated that BGA-4 still had good stability and removal ability after three cycles. Table 1 displays a comparison of efficiency regarding the removal of MO by PDS activation systems in this work and several reported relative studies, which indicated that the BGA-4/SSL/PDS system is a potential approach for dyeing wastewater treatment.

2.6. Role of Reactive Oxidizing Species in the BGA-4/SSL/PDS System

A chemical quenching experiment was performed to investigate the dominant reactive species in the BGA-4/SSL/PDS system. Initially, ethanol (EtOH, 20 mM), tert-butanol (TBA, 20 mM), p-benzoquinone (20 mM), ethylene diamine tetraacetic acid (EDTA), and furfuryl alcohol (20 mM) were employed as the radical scavengers of $SO_4\cdot^-$, ·OH, $O_2\cdot^-$, h^+, and $^1O_2$ to the BGA-4/SSL/PDS system. As shown in Figure 10a, the degradation rates of MO were 73.8%, 81.2%, 48.3%, 72.4%, and 50.2% after 60 min, respectively. EtOH, TBA, and EDTA only showed 16.1%, 8.7%, and 17.5% inhibition in MO degradation, respectively,

suggesting the insignificant role of free radicals ($SO_4\cdot^-$, ·OH, and h^+). In addition, furfuryl alcohol and p-benzoquinone caused the degradation rate of MO to significantly decrease by 28.4% and 25.4%, indicating that $^1O_2$ and $O_2\cdot^-$ played a vital role in MO degradation. $^1O_2$ might be generated though the nucleophilic addition with the aid of the activation of C-O groups to PDS [44]. The formation of $O_2\cdot^-$ was produced through the reaction between the photo-induced electron produced by BiOCl and the dissolved oxygen under simulated sunlight irradiation. The contribution rate of free radicals on MO removal was in the sequence of $^1O_2 > O_2\cdot^- > h^+ > SO_4\cdot^- >$ ·OH in the BGA-4/SSL/PDS system.

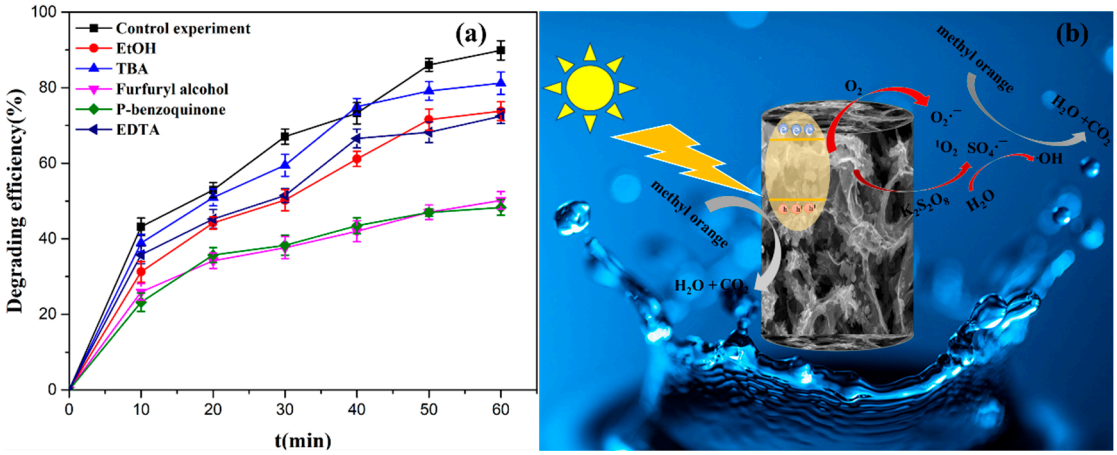


Figure 10. The effect of quenching agents (20 mM) on the degradation efficiency of MO (**a**) and the schematic mechanism of MO degradation (**b**) in the BGA-4/SSL/PDS system (reaction conditions: 0.4 g/L BGA-4, 75 mg/L PDS, 300 W xenon lamp, and C_0 = 15 mg/L).

Table 1. Comparison of efficiency of removing MO in similar catalytic systems.

Process	Light Source	MO Concentration	Catalyst Dosage	PDS Concentration	Degradation Efficiency	Reaction Time	Ref.
GO/PDS/ES	Tungsten-halogen lamp (250 W)	1.5 mM	6 mg·L^{-1}	0.05 mM	77%	240 min	[45]
P25-TiO_2/ZnO/PDS	Tungsten lamp (100 W)	20 mg/L	0.5 g/L	3 ppm	82%	240 min	[46]
ZnO/$AgFeO_2$/PDS	Visible light (LED 50 W)	1×10^{-5} M	0.4 g/L	1.48 mM	70%	300 min	[47]
TiO_2/Fe_3O_4/PDS	UV light (300 W)	20 mg/L	0.4 g/L	60 mM	99.5%	150 min	[48]
Fe_0/PDS	solar	10 mg/L	100 mg/L	360 mg/L	95%	120 min	[49]
BGA-4/PDS	simulated sunlight (Xe 300 W)	15 mg/L	0.4 g/L	0.075 g/L	89.9%	60 min	This study

Multiple pathways were responsible for the MO degradation process (Equations (1)–(6)), and the schematic mechanism is shown in Figure 10b. Firstly, MO molecules were adsorbed on the surface of BGA-4 and then degraded by various reactive oxidizing species. The photo-induced electron reacted with $S_2O_8^{2-}$ and the dissolved oxygen in the solution, respectively. The oxidizing species generated by the above reactions led to the degradation of MO. The rGO thin sheets in BGA-4 could prevent the recombination of photo-induced electrons (e) and holes (h^+), which is of benefit to the removal of MO in the BGA-4/SSL/PDS system.

$$hv \xrightarrow{BGA-4} e + h^+ \quad (1)$$

$$e + S_2O_8^{2-} \rightarrow SO_4^{-}\cdot + SO_4^{2-} \quad (2)$$

$$SO_4^{-}\cdot + H_2O \rightarrow HO\cdot + SO_4^{2-} + H^+ \quad (3)$$

$$e + O_2 \rightarrow O_2^- \cdot \quad (4)$$

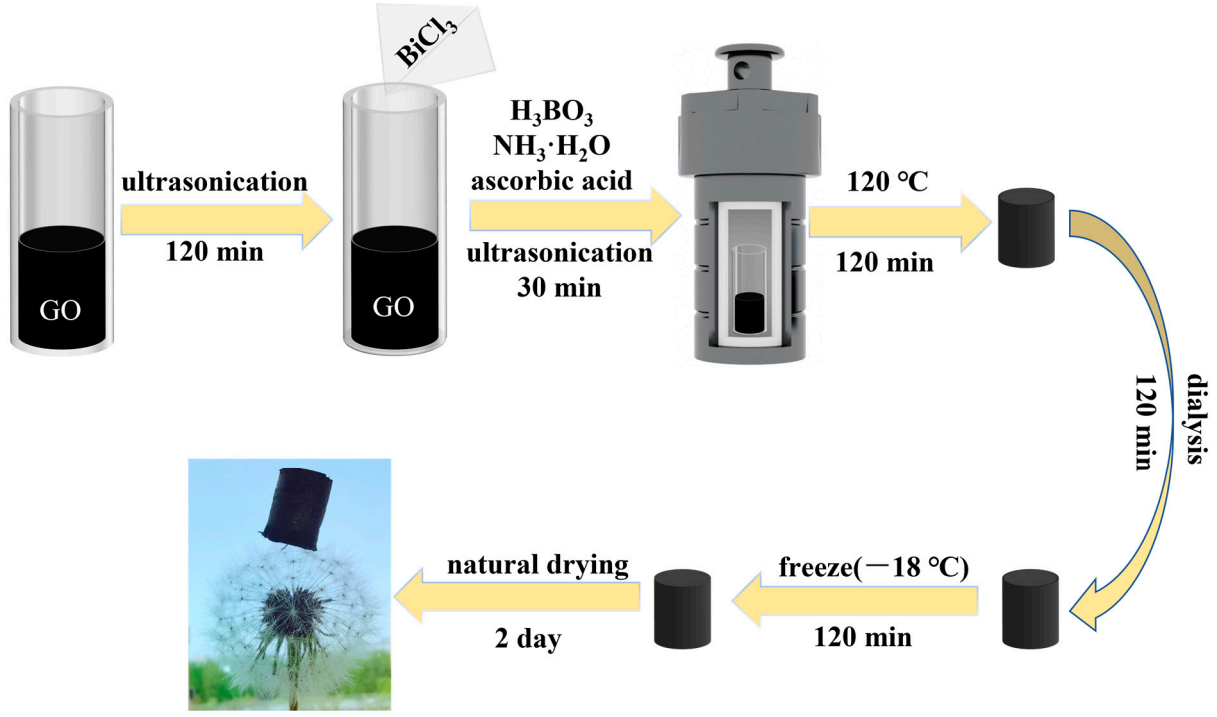
$$BGA-4 + S_2O_8^{2-} + H^+ \rightarrow {}^1O_2 + SO_4^{2-} + H_2O \quad (5)$$

$$MO + {}^1O_2/O_2^- \cdot /h^+/SO_4^- \cdot /HO \cdot \rightarrow \text{Degradation products} \quad (6)$$

3. Materials and Methods

3.1. Synthesis of GA and BiOCl/GA Composite

GO was prepared from natural graphite powder by means of a modified Hummers method [50]. A total of 25 mg of GO powder was dispersed in 5 mL of deionized water and ultrasonically treated for 2 h. The BGA (BiOCl/GA) with different BiOCl concentrations were fabricated in situ by a simple hydrothermal method. The mass percent concentration of BiOCl in the BGA sample was 5%, 10%, 15%, 20%, and 25%, respectively. In brief, certain quantities of $BiCl_3$, 38 µL $NH_3 \cdot H_2O$, 25 mg $Na_2B_4O_7 \cdot 10H_2O$, and 50 mg ascorbic acid were added successively into GO solution and dispersed by ultrasound for 0.5 h. The homogeneous mixture was quickly poured into a Teflon-lined stainless-steel autoclave and maintained at 120 °C for 2 h. The as-formed hydrogel was immersed in 1% ethyl alcohol solution for 2 h then frozen at −18 °C for 2 h and air-dried for 48 h to obtain the ultra-light and compressible BGA. The preparation scheme of BGA was shown in Scheme 1. Different mass proportions of BGA hybrids (5%, 10%, 15%, 20%, and 25%) were named as BGA-1, BGA-2, BGA-3, BGA-4, and BGA-5, respectively. GA was synthesized by the same procedure without adding $BiCl_3$.



Scheme 1. The preparation diagrammatic drawing of BGA.

3.2. Characterization

The structures of the samples were examined by X-ray diffraction (XRD, Rigaku/Smart LabSE). The morphology was evaluated by scanning electron microscopy (SEM; FEI-NOVA NANOSEM 230 (EDS X-MAX50)). X-ray photoelectron spectroscopic (XPS, Thermo Scientific ESCALAB Xi+) analyses were performed. An adsorption analyzer (BET, BELSORP MaxII) was used to calculate the specific surface area. Raman analysis was carried out at a wavelength of 514 nm (Ar-ion laser) using a Raman spectrometer (Raman, SPEX-1403). In-

frared spectra were acquired with a Fourier-transform infrared (FT-IR) spectrometer (FT-IR, IRTracer 100). Electrochemical impedance spectroscopy was studied via an electrochemical system (EIS, CHI E660).

3.3. MO Degradation Procedure

The activation performance for PDS of the prepared GA and BGA composites towards MO solution (15 mg/L) was evaluated under simulated sunlight irradiation at ambient temperature (14 ± 1 °C). Briefly, the activator was directly put into 50 mL MO wastewater; it took 40 min to achieve an adsorption–desorption equilibrium. Afterwards, the cooling water system, the blower system, and the 300 W xenon lamp (100 mW/cm^2) were turned on successively before PDS was added. At given reaction time intervals, the concentration of MO was estimated by a UV–Vis spectrophotometer (1901PC) according to the absorbance at 464 nm. The effects of BiOCl ratio, PDS concentration, activator dosage, initial pH of solution, and coexisting ions on the degradation of MO were investigated, respectively.

4. Conclusions

The multi-functional BiOCl/GA composites were successfully fabricated by the hydrothermal method and through a facile self-assemble approach. Characterization results indicated that BGA-4 composite aerogel possessed a 3D interconnected porous network structure and superior photocatalytic activity in the presence of PDS under simulated sunlight irradiation. The degradation rate constant of MO by the BGA-4/SSL/PDS system (3.56×10^{-2} min^{-1}) was 5.61 times that of the GA/SSL/PDS system (6.35×10^{-3} min^{-1}). The production and rapid electron transfer of photogenic electrons played a vital role in MO removal in the BGA-4/SSL/PDS system. The quenching experiments affirmed that the contribution of reactive species was in a sequence of $^1O_2 > O_2\cdot^- > h^+ > SO_4\cdot^- > \cdot OH$. The catalyst BGA-4 also exhibited excellent stability, high separation capability, and reusability potential. Therefore, the present study not only illustrated an in situ synthesis method for 3D macrostructure BGA-4 but also presented a potential BGA-4/SSL/PDS system for the highly efficient treatment of waste dyeing water.

Author Contributions: Methodology, Y.L.; Validation, C.L.; Investigation, Y.Z.; Resources, S.Y.; Data curation, C.C.; Writing—original draft, D.Z.; Writing—review & editing, Q.C. All authors have read and agreed to the published version of the manuscript.

Funding: This research was funded by the NSFC (Grants No. 22076039, 51808199), the China Postdoctoral Science Foundation (Grant No. 2018M630825, 2019T120624), and the Excellent Science and Technology Innovation Team of Henan Normal University (2021TD03).

Institutional Review Board Statement: Not applicable.

Informed Consent Statement: Not applicable.

Data Availability Statement: Not applicable.

Conflicts of Interest: The authors declare no conflict of interest.

Sample Availability: Samples are available from the author.

References

1. Lv, T.; Wang, L.; Xie, H.; Zhang, X.; Zhang, Y. Evolutionary overview of water resource management (1990–2019) based on a bibliometric analysis in Web of Science. *Ecol. Inform.* **2021**, *61*, 101218. [CrossRef]
2. Wang, Y.; Danook, S.H.; Al-Bonsrulah, H.; Veeman, D.; Wang, F. A Recent and Systematic Review on Water Extraction from the Atmosphere for Arid Zones. *Energies* **2022**, *15*, 421. [CrossRef]
3. Valavanidis, A. "Blue Planet" is Expected to Experience Severe Water Shortages? How Climate Change And Rising Temperatures Are Threatening The Global Water Cycle On Earth. 2019. Available online: http://chem-tox-ecotox.org/scientificreviews/ (accessed on 13 May 2023).
4. Lu, X.; Yang, B.; Chen, J.; Sun, R. Treatment of wastewater containing azo dye reactive brilliant red X-3B using sequential ozonation and upflow biological aerated filter process. *J. Hazard. Mater.* **2009**, *161*, 241–245. [CrossRef]

5. Shi, Y.; Yang, Z.; Xing, L.; Zhou, J.; Ren, J.; Ming, L.; Hua, Z.; Li, X.; Zhang, D. Ethanol as an efficient cosubstrate for the biodegradation of azo dyes by Providencia rettgeri: Mechanistic analysis based on kinetics, pathways and genomics. *Bioresour. Technol.* **2020**, *319*, 124117. [CrossRef]
6. Matabola, K.P.; Mokhena, T.C.; Sikhwivhilu, K.; Mokhothu, T.H.; Mochane, M.J. Poly(vinyl alcohol) (PVA)-based nanofibers materials for azo dye adsorption: An overview. *Int. J. Environ. Sci. Technol.* **2022**, *20*, 7029–7054. [CrossRef]
7. Quaff, A.R.; Venkatesh, S.; Venkatesh, K. Degradation of Azo Dye by Ozone Oxidation: Cost Analysis and Buffering Effects on Dye Decomposition. *Natl. Acad. Sci. Lett.* **2021**, *44*, 339–341. [CrossRef]
8. Munoz, M.; Pedro, Z.D.; Casas, J.A.; Rodriguez, J.J. Preparation of magnetite-based catalysts and their application in heterogeneous Fenton oxidation—A review. *Appl. Catal. B Environ.* **2015**, *176–177*, 249–265. [CrossRef]
9. Nie, C.; Dai, Z.; Meng, H.; Duan, X.; Qin, Y.; Zhou, Y.; Ao, Z.; Wang, S.; An, T. Peroxydisulfate activation by positively polarized carbocatalyst for enhanced removal of aqueous organic pollutants. *Water Res.* **2019**, *166*, 115043. [CrossRef] [PubMed]
10. Yu, Q.; Zhang, Y.; Liu, G.; Shi, J.; Wen, T.; Liu, M. A magnetic sludge carbon combined persulfate-based ISCO system for leachate-contaminated groundwater remediation. *J. Water Process Eng.* **2022**, *50*, 103331. [CrossRef]
11. Zhang, J.; Ma, J.; Zou, J.; Chi, H. Spectrophotometric determination of persulfate anion via oxidative depolarization of methyl orange induced by ferrous ions. *Desalination Water Treat.* **2016**, *57*, 25235–25241. [CrossRef]
12. Xu, N.; Hu, C.; Zhu, Z.; Wang, W.; Peng, H.; Liu, B. Establishment of a novel system for photothermal removal of ampicillin under near-infrared irradiation: Persulfate activation, mechanism, pathways and bio-toxicology. *J. Colloid Interface Sci.* **2023**, *640*, 472–486. [CrossRef]
13. Liu, B.; Huang, B.; Wang, Z.; Tang, L.; Ji, C.; Zhao, C.; Feng, L.; Feng, Y. Homogeneous/Heterogeneous Metal-Catalyzed Persulfate Oxidation Technology for Organic Pollutants Elimination: A Review. *J. Environ. Chem. Eng.* **2023**, *11*, 109586. [CrossRef]
14. Liu, S.; Wang, J.; Zhang, Z.; Dou, M.; Huo, K.; Ding, G.; Zhou, Y.; Qiao, C. Persulfate activation by sludge-derived biochar for efficient degradation of 2,4-dichlorophenol: Performance and mechanism. *Environ. Sci. Pollut. Res.* **2023**, *30*, 45259–45273. [CrossRef] [PubMed]
15. Cheng, X.; Guo, H.; Zhang, Y.; Wu, X.; Liu, Y. Non-photochemical production of singlet oxygen via activation of persulfate by carbon nanotubes. *Water Res.* **2017**, *113*, 80–88. [CrossRef] [PubMed]
16. Luo, S.; Samad, Y.A.; Chan, V.; Liao, K. Cellular Graphene: Fabrication, Mechanical Properties, and Strain-Sensing Applications. *Matter* **2019**, *1*, 1148–1202. [CrossRef]
17. Peng, W.; Liu, S.; Sun, H.; Yao, Y.; Zhi, L.; Wang, S. Synthesis of porous reduced graphene oxide as metal-free carbon for adsorption and catalytic oxidation of organics in water. *J. Mater. Chem. A* **2013**, *1*, 5854–5859. [CrossRef]
18. Karbasi, S. Improving visible light photocatalytic inactivation of E. coli by inducing highly efficient radical pathways through peroxymonosulfate activation using 3-D, surface-enhanced, reduced graphene oxide (rGO) aerogels. *Chem. Eng. J.* **2020**, *396*, 125189. [CrossRef]
19. Ma, D.; Li, J.; Liu, A.; Chen, C. Carbon Gels-Modified TiO_2: Promising Materials for Photocatalysis Applications. *Materials* **2020**, *13*, 1734. [CrossRef]
20. Cai, J.; Liu, W.; Li, Z. One-pot self-assembly of Cu_2O/RGO composite aerogel for aqueous photocatalysis—ScienceDirect. *Appl. Surf. Sci.* **2015**, *358*, 146–151. [CrossRef]
21. Chen, F.; Li, S.; Chen, Q.; Zheng, X.; Liu, P.; Fang, S. 3D graphene aerogels-supported Ag and Ag@Ag_3PO_4 heterostructure for the efficient adsorption-photocatalysis capture of different dye pollutants in water. *Mater. Res. Bull.* **2018**, *105*, 334–341. [CrossRef]
22. Li, M.; Huang, S.; Li, H.; Feng, X.; Wang, Y.; Wang, C.; Ma, Y.; Guo, T.; Zhang, L.; He, Y. Unprecedented Eighteen-Faceted BiOCl with a Ternary Facet Junction Boosting Cascade Charge Flow and Photo-redox. *Angew. Chem.* **2019**, *58*, 9517–9521. [CrossRef] [PubMed]
23. Xza, B.; Xx, A.; Jc, A.; Yi, W.A.; Hw, B. Understanding the effects of co-exposed facets on photocatalytic activities and fuel desulfurization performance in BiOCl singlet-crystalline sheets. *J. Hazard. Mater.* **2020**, *391*, 122198.
24. Zhang, J.; Wang, Z.; Fan, M.; Tong, P.; Sun, J.; Dong, S.; Sun, J. Ultra-light and compressible 3D BiOCl/ RGO aerogel with enriched synergistic effect of adsorption and photocatalytic degradation of oxytetracycline—ScienceDirect. *J. Mater. Res. Technol.* **2019**, *8*, 4577–4587. [CrossRef]
25. Zhang, J.; Wang, Z.; Chu, L.; Chen, R.; Fan, M. Unified photoelectrocatalytic microbial fuel cell harnessing 3D binder-free photocathode for simultaneous power generation and dual pollutant removal. *J. Power Sources* **2021**, *481*, 229133. [CrossRef]
26. Yang, J.; Chen, D.; Zhu, Y.; Zhang, Y.; Zhu, Y. 3D-3D porous Bi_2WO_6/graphene hydrogel composite with excellent synergistic effect of adsorption-enrichment and photocatalytic degradation. *Appl. Catal. B Environ. Int. J. Devoted Catal. Sci. Its Appl.* **2017**, *205*, 228–237. [CrossRef]
27. Xue, Y.; Shi, J.; Feng, L.; Li, C.; Liang, W. A three-dimensional BiOBr/RGO heterostructural aerogel with enhanced and selective photocatalytic properties under visible light. *Appl. Surf. Sci.* **2017**, *396*, 1775–1782.
28. Dong, S.; Xia, L.; Chen, X.; Cui, L.; Fan, M. Interfacial and electronic band structure optimization for the adsorption and visible-light photocatalytic activity of macroscopic $ZnSnO_3$/graphene aerogel. *Compos. Part B Eng.* **2021**, *215*, 108765. [CrossRef]
29. Wang, Q.; Wang, W.; Zhong, L.; Liu, D.; Cao, X.; Cui, F. Oxygen vacancy-rich 2D/2D BiOCl-g-C_3N_4 ultrathin heterostructure nanosheets for enhanced visible-light-driven photocatalytic activity in environmental remediation. *Appl. Catal. B Environ. Int. J. Devoted Catal. Sci. Its Appl.* **2018**, *220*, 290–302. [CrossRef]

30. Shinde, N.M.; Xia, Q.X.; Yun, J.M.; Singh, S.; Mane, R.S.; Kim, K.H. A binder-free wet chemical synthesis approach to decorate nanoflowers of bismuth oxide on Ni-foam for fabricating laboratory scale potential pencil-type asymmetric supercapacitor device. *Dalton. Trans.* **2017**, *46*, 6601–6611. [CrossRef]
31. Li, F.Q.; Sun, B.H.; Qin, Y.L.; Liu, X.Y.; Liu, Z.Y.; Ni, D.R.; Xiao, B.L.; Ma, Z.Y. Enhanced photocatalysis performance of BiOCl/graphene modified via polyvinylpyrrolidone. *Vac. Technol. Appl. Ion Phys. Int. J. Abstr. Serv. Vac. Sci. Technol.* **2021**, *184*, 109857. [CrossRef]
32. Zz, A.; Hx, B.; Dl, A.; Js, A.; Dxa, B. Facile preparation and photocatalytic activity of oxygen vacancy rich BiOCl with {001} exposed reactive facets. *Appl. Surf. Sci.* **2019**, *463*, 1011–1018.
33. Li, Y.; Li, D.; Qin, T.; Shi, Z.; Fu, P.; Xiong, D.; Dong, X. A comparative study of proton conduction between two new Cd(II) and Co(II) complexes and in vitro antibacterial study of the Cd(II) complex. *Appl. Organomet. Chem.* **2023**, *37*, e6920. [CrossRef]
34. Kai, H.; Chen, G.; Zeng, G.; Chen, A.; Liang, H. Three-dimensional graphene supported catalysts for organic dyes degradation. *Appl. Catal. B: Environ.* **2018**, *228*, 19–28.
35. Zhang, S.; Song, S.; Gu, P.; Ma, R.; Wei, D.; Zhao, G.; Wen, T.; Jehan, R.; Hu, B.; Wang, X. Visible-light-driven activation of persulfate over cyano and hydroxyl group co-modified mesoporous g-C_3N_4 for boosting bisphenol A degradation. *J. Mater. Chem. A Mater. Energy Sustain.* **2019**, *7*, 5552–5560. [CrossRef]
36. Xiao, C.; Wdo, C.; Phz, D.; Rdw, E.; Ttla, B. Surface construction of nitrogen-doped chitosan-derived carbon nanosheets with hierarchically porous structure for enhanced sulfacetamide degradation via peroxymonosulfate activation: Maneuverable porosity and active sites—ScienceDirect. *Chem. Eng. J.* **2020**, *382*, 122908.
37. Hasanvandian, F.; Shokri, A.; Moradi, M.; Kakavandi, B.; Setayesh, S.R. Encapsulation of spinel $CuCo_2O_4$ hollow sphere in V2O5-decorated graphitic carbon nitride as high-efficiency double Z-type nanocomposite for levofloxacin photodegradation. *J. Hazard. Mater.* **2021**, *423*, 127090. [CrossRef] [PubMed]
38. Moradi, M.; Kakavandi, B.; Bahadoran, A. Intensification of persulfate-mediated elimination of bisphenol A by a spinel cobalt ferrite-anchored g-C_3N_4 S-scheme photocatalyst; Catalytic synergies and mechanistic interpretation. *Sep. Purif. Technol.* **2022**, *285*, 120313. [CrossRef]
39. Liu, B.; Qiao, M.; Wang, Y.; Wang, L.; Gong, Y.; Guo, T.; Zhao, X. Persulfate enhanced photocatalytic degradation of bisphenol A by g-C_3N_4 nanosheets under visible light irradiation. *Chemosphere* **2017**, *115*, 115–122. [CrossRef]
40. Zhu, S.; Li, X.; Kang, J.; Duan, X.; Wang, S. Persulfate activation on crystallographic manganese oxides: Mechanism of singlet oxygen evolution for nonradical selective degradation of aqueous contaminants. *Environ. Sci. Technol.* **2018**, *53*, 307–315. [CrossRef]
41. Dong, S.; Cui, L.; Liu, C.; Zhang, F.; Li, K.; Xia, L.; Su, X.; Feng, J.; Zhu, Y.; Sun, J. Fabrication of 3D ultra-light graphene aerogel/Bi_2WO_6 composite with excellent photocatalytic performance: A promising photocatalysts for water purification. *J. Taiwan Inst. Chem. Eng.* **2019**, *97*, 288–296. [CrossRef]
42. Duan, X.; Ao, Z.; Zhou, L.; Sun, H.; Wang, G.; Wang, S. Occurrence of radical and nonradical pathways from carbocatalysts for aqueous and nonaqueous catalytic oxidation. *Appl. Catal. B Environ.* **2016**, *188*, 98–105. [CrossRef]
43. Gu, M.; Farooq, U.; Lu, S.; Zhang, X.; Qiu, Z.; Sui, Q. Degradation of trichloroethylene in aqueous solution by rGO supported nZVI catalyst under several oxic environments. *J. Hazard. Mater.* **2018**, *349*,, 35–44. [CrossRef]
44. Liu, C.; Liu, S.; Liu, L.; Tian, X.; Liu, L.; Xia, Y.; Liang, X.; Wang, Y.; Song, Z.; Zhang, Y.; et al. Novel Carbon-based Fe-Co Oxides Derived from Prussian Blue Analogues Activating Peroxymonosulfate: Refractory Drugs Degradation without Metal Leaching. *Chem. Eng. J.* **2019**, *379*, 122274. [CrossRef]
45. Govindan, K.; Suresh, A.K.; Sakthivel, T.; Murugesan, K.; Jang, A. Effect of peroxomonosulfate, peroxodisulfate and hydrogen peroxide on graphene oxide photocatalytic performances in methyl orange dye degradation. *Chemosphere* **2019**, *237*, 124479. [CrossRef] [PubMed]
46. Joshaghani, M.; Yazdani, D.; Zinatizadeh, A.A. Statistical modeling of p-nitrophenol degradation using a response surface methodology (RSM) over nano zero-valent iron-modified Degussa P25-TiO_2/ZnO photocatalyst with persulfate. *J. Iran. Chem. Soc.* **2017**, *14*, 2449–2456. [CrossRef]
47. Sabri, M.; Habibi-Yangjeh, A.; Chand, H.; Krishnan, V. Heterogeneous photocatalytic activation of persulfate ions with novel ZnO/$AgFeO_2$ nanocomposite for contaminants degradation under visible light. *J. Mater. Science. Mater. Electron.* **2021**, *32*, 4272–4289. [CrossRef]
48. Song, T.; Gao, Y.; Hu, R.; Li, G.; Yu, X. Degradation of Methyl Orange in Aqueous Solution via Magnetic TiO_2/Fe_3O_4 Conjugated with Persulfate. *Water Air Soil Pollut.* **2023**, *234*, 508. [CrossRef]
49. Munkoeva, V.A.; Sizykh, M.R.; Batoeva, A.A. Iop. Photo Degradation of Methyl Orange by Persulfate Activated with Zero Valent Iron. In Proceedings of the International Conference on Construction, Architecture and Technosphere Safety (ICCATS), Chelyabinsk, Russia, 21–22 September 2017.
50. Hummers, W.S., Jr.; Offeman, R.E. Preparation of Graphitic Oxide. *J. Am. Chem. Soc.* **1958**, *80*, 1339. [CrossRef]

Disclaimer/Publisher's Note: The statements, opinions and data contained in all publications are solely those of the individual author(s) and contributor(s) and not of MDPI and/or the editor(s). MDPI and/or the editor(s) disclaim responsibility for any injury to people or property resulting from any ideas, methods, instructions or products referred to in the content.